

Revealing Fano Combs in Directional Mie Scattering

Javier Marmolejo (✉ javier.marmolejo@physics.gu.se)

University of Gothenburg <https://orcid.org/0000-0002-3665-7931>

Adriana Canales

Chalmers University of Technology <https://orcid.org/0000-0002-9803-6559>

Dag Hanstorp

University of Gothenburg

Ricardo Méndez-Fragoso

Universidad Nacional Autónoma de México

Article

Keywords: Directional Mie Scattering, Fano Combs, directional Mie spectrum, constructive interference, computational simulations

Posted Date: December 17th, 2021

DOI: <https://doi.org/10.21203/rs.3.rs-1100661/v1>

License:  This work is licensed under a Creative Commons Attribution 4.0 International License.

[Read Full License](#)

Revealing Fano Combs in Directional Mie Scattering

Javier Tello Marmolejo^{1,*}, Adriana Canales², Dag Hanstorp¹, and Ricardo Méndez-Fragoso³

¹Department of Physics, University of Gothenburg, SE-412 96 Gothenburg, Sweden

²Department of Physics, Chalmers University of Technology, SE-412 96, Göteborg, Sweden

³Facultad de Ciencias, Universidad Nacional Autónoma de México, Av. Universidad 3000, Circuito Exterior S/N Delegación Coyoacán, C.P. 04510 Ciudad Universitaria, Ciudad de México, México

*javier.marmolejo@physics.gu.se

November 25, 2021

Abstract

The constructive interference of light reflecting on the inner surface of a dielectric sphere results in a rich Mie scattering spectrum. Each resonance can be understood through a quantum-mechanical analogy, while the structure of the full spectrum is predicted to be a series of Fano resonances. However, the overlap of all the different modes results in such a complex spectrum that an intuitive understanding of the full, underlying structure is still missing. Here we present a *directional Mie spectrum* obtained by selecting a particular polarization and direction of the scattering of levitating water droplets. We find a significantly simplified spectrum organized in distinct, consecutive *Mie Fano Combs* composed of equidistant resonances that smoothly evolve from wide Lorentzians into sharp Fano profiles. We then fully explain all these characteristics by expanding on the quantum-mechanical analogy. This makes it possible to understand Mie spectra intuitively without the need for computational simulations.

Main

The scattering of an electromagnetic wave by a dielectric sphere was first calculated by Gustav Mie in 1908.¹ Despite the simplicity of a sphere and a plane wave, this problem leads to a rich spectrum of radius-dependant resonances called Whispering Gallery Modes or Mie resonances. A common explanation of these resonances is that light internally reflects around the sphere, and resonances appear every time the circumference is a multiple of the wavelength inside the material (λ/n).²⁻⁶

Mie resonances are not only found in spheres but also in other geometries such as discs⁷ or toroids.⁶ Their quality factors can be several orders of magnitude higher than Fabry-Perot resonators,⁴ making them ideal as sensors^{6,8} or as laser cavities.⁹ Even more so, they are suitable for obtaining self-hybridized polaritons, for potentially changing the material properties of a sample.^{10,11}

These resonances are particularly relevant in the field of optical trapping. In fact, Arthur Ashkin observed Mie resonances in the scattering force of an optically levitated solid micro-particle.¹²

For solid spheres, the radius is fixed and Mie resonances can be found by varying the trapping wavelength of the laser, but the spectrum range is then strongly limited by the tunable range of the laser. Much wider Mie spectra can be achieved using evaporating droplets at a constant wavelength. However, stable optical trapping of evaporating droplets can be complicated since the weight and cross-section of the laser trap varies greatly as it shrinks. This changes the optical forces, causing the droplet to drift in the trap or be lost. One solution is to use liquids with slow evaporation rates such as glycerol¹³ or salt-water solution in a humid environment.¹⁴ Droplets can also be trapped in electric quadrupole traps and probed by LEDs¹⁵ or lasers.¹⁶ Nevertheless, providing a consistent laser excitation and stable trapping for shrinking, micrometric particles is still a challenge.

Commonly, the resulting spectra are compared to numerical simulations obtained from Mie theory,^{13,14,17–19} which usually show excellent agreement. However, although the simulations can reproduce the experimental spectra, they do not reveal an intuitive understanding of the complicated structure of the multitude of overlapping sharp and wide resonances.

Mie resonances can also be understood through a quantum mechanical analogy.^{2,3} By choosing an appropriate potential for the Schrödinger equation, it turns out to be identical to the equation that governs the scattering of a particle in the radial coordinate. This allows us to understand individual resonances with the tools from quantum mechanics. However, Mie spectra are a result of so many overlapping resonances that a full understanding through this analogy has fallen short.

The Mie spectrum is predicted to be composed of a series of Fano resonances,^{20–23} but Fano resonances in simple spheres are difficult to detect due to dissipative losses,²⁴ and because Fano resonances are forbidden for a wide angular scattering.²⁵ For this reason, individual Mie Fano resonances have only been observed using special geometries such as ring/disk cavities⁷ or multilayer nanoshells.²⁶ Despite this, *directional Fano* resonances in simple spheres should indeed be possible to observe in a singled out direction and polarization.²⁵

In this paper, we built a precise optical trap that allowed us to consistently excite Mie resonances for shrinking droplets and we measured their scattering on a specific direction and polarization. Thus, we disentangled the Mie spectrum leading to the emergence of structured resonances all the way down to their lowest orders for sub-micrometric spheres. We show that Mie resonances are indeed a series of evolving, equidistant Fano resonances organized in consecutive *Mie Fano Combs*. Each comb shows a series of resonances that raise and fall in amplitude and smoothly turn from wide Lorentzians to sharp Fano profiles. We then provide a theoretical understanding by expanding the previous quantum-mechanical analogies in a way where it is now possible to fully and intuitively explain the now simplified *directional Mie spectrum* and its *Fano Comb* structure.

Directional Mie Spectrum

We built a counter-propagating optical trap where we levitated water droplets in air and measured the scattering intensity of the droplets as they evaporated. Our trap is capable of trapping droplets from $\simeq 6 \mu\text{m}$ down to full evaporation with a constant position. By keeping the shrinking droplet stable with respect to the laser trap, we ensured a consistent electromagnetic excitation throughout the process. We set both beams of the counter-propagating trap to be vertically polarized. The droplet scatters laser light in all directions, out of which we selected the horizontal polarization of the scattering perpendicular to the laser trap with a small solid angle (see Methods).

We can write the polarization components I_ϕ and I_θ of the scattering of a sphere with an incident plane wave traveling along the z-axis with polarization along the x-axis as^{25,27}

$$I_\phi = \frac{\lambda^2}{4\pi^2 r^2} |S_1|^2 \sin^2(\phi), \quad I_\theta = \frac{\lambda^2}{4\pi^2 r^2} |S_2|^2 \cos^2(\phi), \quad (1)$$

where r , θ , and ϕ are the spherical coordinates with the origin at the center of the sphere.

In the direction we observe ($\phi \simeq \pi/2$), $\sin^2(\phi) \simeq 1$ and $\cos^2(\phi) \simeq 0$. Indeed we observe that

$I_\phi \gg I_\theta$. We selected the dimmer scattering component, I_θ , which depends on

$$S_2 = \sum_{\ell} \frac{2\ell + 1}{\ell(\ell + 1)} [a_{\ell}\tau_{\ell}(\cos\theta) + b_{\ell}\pi_{\ell}(\cos\theta)] , \quad (2)$$

$$\pi_{\ell}(\cos\theta) = \frac{P_{\ell}^1(\cos\theta)}{\sin\theta} , \quad \tau_{\ell}(\cos\theta) = \frac{d}{d\theta} P_{\ell}^1(\cos\theta) . \quad (3)$$

P_{ℓ}^1 are the associated Legendre polynomials, and a_{ℓ} and b_{ℓ} are the *scattering coefficients* that range from 0 to 1 related to the electric and magnetic polarizabilities, respectively. The resonances result from two linearly independent modes inside the sphere, the spherical Transverse Electric (TE) and Transverse Magnetic (TM) modes. For a TM resonance $a_{\ell} = 1$ and for a TE resonance $b_{\ell} = 1$. For ℓ odd $\tau_{\ell}(\cos(\pi/2)) = 0$ and for ℓ even $\pi_{\ell}(\cos(\pi/2)) = 0$. It follows that for each ℓ we only observe either the TE or the TM resonant mode, which would otherwise overlap. This selection of one of the modes gives a significantly simplified *directional Mie scattering spectrum*. Note that the dependence of the radius of the droplet is included in the scattering coefficients a_{ℓ} and b_{ℓ} . The scattering, $I_{\theta}(t)$, of a shrinking sphere is shown in Fig. 1a.

Clearly, time is not the relevant parameter, but size. To calculate the size of the droplet during the evaporation, we projected the other component of the polarization, I_{ϕ} , onto a screen and filmed it. This far-field scattering of a trapped sphere results in a fringe pattern since the sphere scatters predominantly from its poles along the direction of the laser.^{28,29} Fig. 1b shows interference

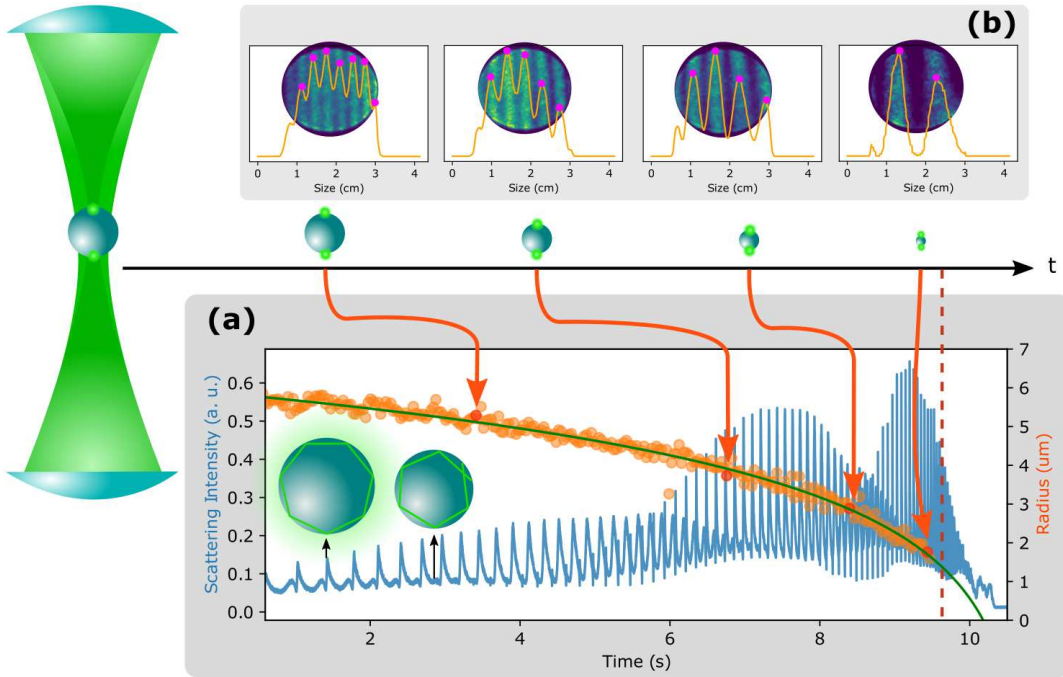


Figure 1: Simultaneous measurement of a typical *directional Mie scattering spectrum* and the absolute size of the evaporating water droplet. **(a)** Scattering intensity, I_θ , of the droplet (blue) and radius of the droplet (orange dots) with a logarithmic fit (green). As the the evaporation of the droplet accelerates, the Mie resonances occur consecutively faster. After the red dashed line, the interference pattern becomes too large and the size cannot be calculated from the scattering. **(b)** Far-field interference patterns of a few selected frames of the shrinking droplet used to measure the radius plotted in (a).

patterns for consecutively smaller spheres. A histogram of the intensity (orange line) was used to calculate the distance S between the stripes. We used this “double-slit approximation” to calculate the absolute radius of the droplet, a , using the wavelength, λ , the distance to the screen, d , and the equation

$$a = \frac{2d\lambda}{S(2 + \sqrt{2})} . \quad (4)$$

Fig. 1a shows radius of the droplet in orange and a fit using a logarithmic function in green. We used the fit to obtain the *directional Mie spectrum* as a function of the radius of the droplet.

Mie Fano Comb structure

With the radius now on the x-axis, the resonances from Fig. 1b spread out and a periodic structure appears, shown in Fig. 2a. As opposed to non-directional Mie spectra,^{13,14,17,18} the entire spectrum can be understood as a series of separate resonances where at most two overlap, and each can be clearly identified. We observe three distinct, overlapping combs composed of a series of equidistant resonances. The leftmost comb does not overlap with a new one to its left, meaning that this is the first comb with the lowest order Mie resonances. Resonances for smaller spheres cannot exist since the wavelength becomes comparable to the circumference and light cannot *coil* around the surface of the sphere.

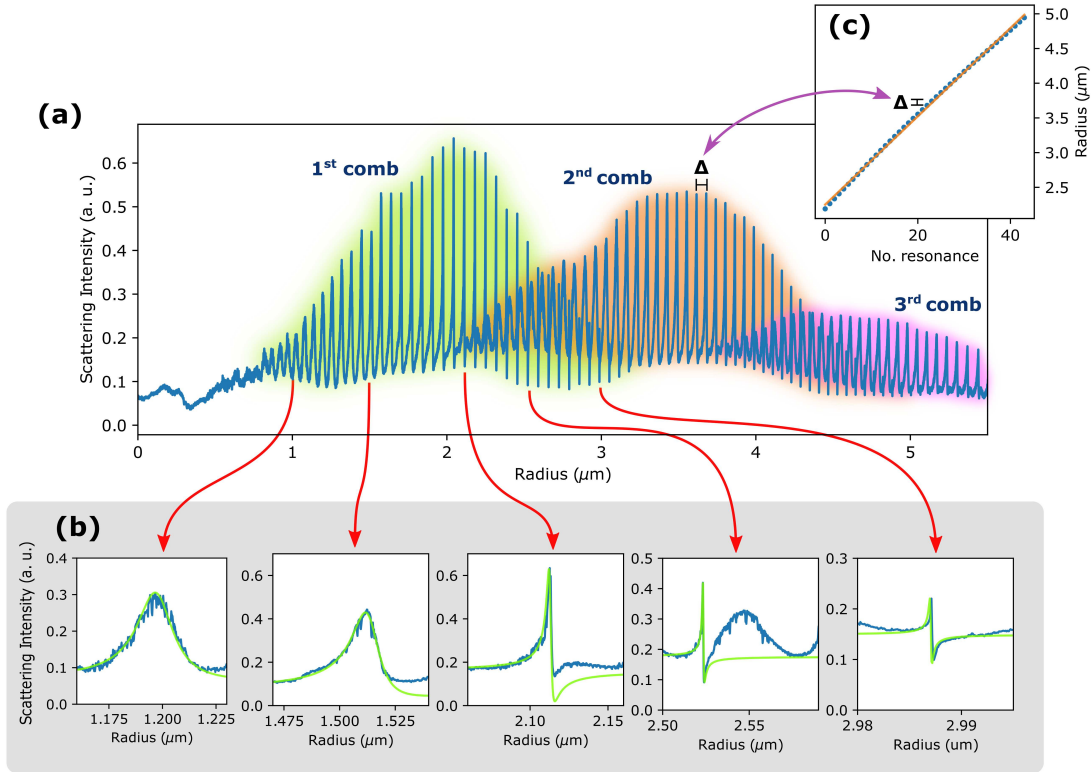


Figure 2: *Fano Comb* structure of the directional Mie scattering. (a) Directional scattering intensity, I_θ , as the droplet shrinks. Highlighted are the first three *combs* composed of equidistant, evolving Fano resonances. (b) Evolution of the resonances from Lorentzians to Fano through five selected segments of the first comb. For each resonance, a fit to the Fano equation, Eq.(5), is shown as a solid green line. (c) The radius obtained from Eq.(5) as a function of the number of the resonance in the second comb. The linear fit (orange) shows the equidistant appearance of the resonances inside a comb.

Each comb is composed of distinct Fano resonances that evolve from being symmetric (Lorentz form) to the dispersive shape that is a signature of a Fano resonance. Fig. 2b shows select resonances fitted using Fano's equation including a non-interacting component of the background²⁰

$$\sigma(\Omega) = D^2 \left[\frac{(q + \Omega)^2}{1 + \Omega^2} \eta + (1 - \eta) \right] , \quad (5)$$

where $q = \cot(\delta)$ is the Fano parameter, δ is the phase shift with the continuum, $\eta \in [0, 1]$ is an interaction coefficient, and $D^2 = 4 \sin^2(\delta)$. Fano resonances are usually written as a function of the energy, E , with $\Omega = 2(E - E_0)/\Gamma$, where Γ is the resonance width and E_0 the energy of the resonance. In this case, we have replaced the energy in Ω with the radius of the sphere.

Fano resonances occur when a resonance interferes with a continuum. Here, we observe *directional Fano resonances*,²⁵ which can be interpreted as non-resonant scattered light ($a_\ell, b_\ell \neq 1$ for all non resonant ℓ 's) interfering with resonant light (b_ℓ or $a_\ell = 1$ for the resonant ℓ) leaving with a phase shift after rotating inside the sphere. The fitting of each individual resonance confirms predictions of Mie scattering being composed of a series of Fano resonances.²⁰⁻²³ Additionally, it unites the wide and sharp resonances commonly observed in Mie scattering spectra as the same phenomenon through a smooth transition of the parameters in Eq.(5).

Fig. 2c shows the constant separation between resonances, where we plotted the center of each resonance in the second comb obtained from the fit of Eq.(5). The slope is $\Delta = 63.6 \pm 2.3$ nm resulting in resonances occurring every change in circumference of $2\pi\Delta = 399 \pm 14$ nm. This supports the interpretation that light coils around the droplet and constructive interference occurs every time the circumference is a multiple of $\lambda/n = 532.0 \text{ nm}/1.333 = 399.1$ nm.

Quantum mechanical analogy

To explain the *Fano Comb* structure we present an analogy between optics and quantum mechanics based on the analogies of Guimaraes² and, particularly, of Johnson.³

From Maxwell's equations, we know that for a non-magnetic, uncharged sphere with radius a , the electric field must follow the equation

$$\nabla \times (\nabla \times \mathbf{E}) - k^2 n^2(r) \mathbf{E} = 0 , \quad (6)$$

where \mathbf{E} is the electric field, $k = 2\pi/\lambda$ the wavenumber, and $n(r)$ the refractive index where, in our case, $n_{water}(r < a) = 1.333$ and $n_{air}(r > a) = 1$. This results in two linearly independent solutions, $M_{\ell,m}(r, \theta, \phi)$ and $N_{\ell,m}(r, \theta, \phi)$, corresponding to the TE and TM modes respectively and given by³

$$M_{\ell,m}(r, \theta, \phi) = \frac{e^{im\phi}}{kr} S_\ell(r) \mathbf{X}_{\ell,m}(\theta) , \quad (7)$$

$$N_{\ell,m}(r, \theta, \phi) = \frac{e^{im\phi}}{k^2 n^2(r)} \left[\frac{1}{r} \frac{\partial T_\ell(r)}{\partial r} \mathbf{Y}_{\ell,m}(\theta) + \frac{1}{r^2} T_\ell(r) \mathbf{Z}_{\ell,m}(\theta) \right] , \quad (8)$$

where $\mathbf{X}_{\ell,m}$, $\mathbf{Y}_{\ell,m}$, and $\mathbf{Z}_{\ell,m}$ are the angular solutions of Eq.(6) with ℓ the main angular momentum number and m the degeneration. In particular, $S_\ell(r)$ satisfies the differential equation

$$\frac{d^2 S_\ell(r)}{dr^2} + \left[k^2 n^2(r) - \frac{\ell(\ell+1)}{r^2} \right] S_\ell(r) = 0 . \quad (9)$$

From now on we will only refer to the TE mode since the treatment for the TM mode is analogous (see Methods).

Eq.(9) is extremely similar to the Schrödinger equation. In fact, if we define the energy as $E = k^2$, and choose a square well potential

$$V(r) = -k^2 [n^2(r) - 1] , \quad (10)$$

then the radial, time-independent Schrödinger equation with a central potential and with $\hbar/2\mu = 1$ becomes

$$-\frac{d^2\Psi(r)}{dr^2} + \left[-k^2[n^2(r) - 1] + \frac{\ell(\ell + 1)}{r^2} \right] \Psi(r) = E\Psi(r) , \quad (11)$$

which is identical to Eq.(9).

With this analogy, we can use the interpretation of resonances from quantum mechanics to understand the resonances we observe. The effective potential is a *wedged potential well* resulting from the sum of a centrifugal potential with ℓ as the quantum number for the angular momentum plus an attractive square well. A bound energy level in this potential can be understood as the light trapped inside the droplet, continuously reflecting on the inside of the surface, where the rotation around the circumference gives the light angular momentum.

Fig. 3a shows four *wedged potential wells* (blue) and their calculated energy levels. Here, a level represents the energy, k^2 , of the laser that would produce a Mie resonance. The dot-dashed line represents the energy of the 532.0 nm trapping laser, and a resonance occurs when one of the energy levels of the well matches the energy of the laser.

Fig. 3b shows the observed scattering for the different resonances. The green fits mark the

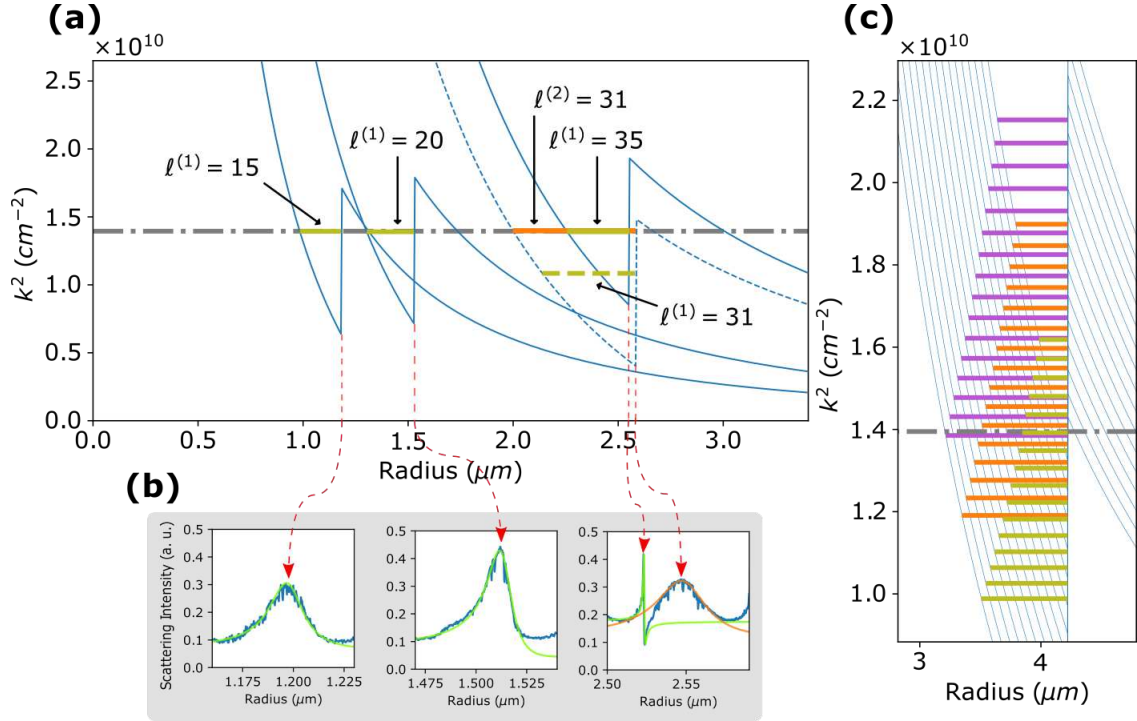


Figure 3: *Fano Comb* structure in the energy levels of a wedged potential well. (a) Selected *wedged potential wells* for the given ℓ s and radii. The superscript defines the index of the energy level inside a wedge, i.e., the $\ell^{(1)}$ s mark the first energy level inside a wedge in green and the $\ell^{(2)}$ s the second one in orange. The wedge for $\ell = 31$ is dashed for better contrast with $\ell = 35$ and its green energy level, $\ell^{(1)} = 31$, is dashed to mark that it is not resonate with the laser. See SI for a video of the energy levels in a growing sphere resonating with the laser. (b) The directional scattering of the droplet (blue) and a fit using Eq.(5). Green fit for the first level, i.e. first comb, and orange for the second comb. (c) All energy levels for a larger drop where the first, second and thirds combs are visible now in the three sets of green, orange and purple levels. These would be the resonances observed when scanning the wavelength for a spheres with fixed radius.

resonances from the first comb and are related to the first energy level inside a wedge, $\ell^{(1)}$. When the well becomes wide enough, an additional energy level appears, $\ell^{(2)}$, and the second comb begins, shown in orange.

The first well, $\ell^{(1)} = 15$, has a narrow barrier, resulting in a wide, Lorentzian resonance. For the next resonant levels, $\ell^{(1)} = 20$ and $\ell^{(1)} = 35$, the barrier becomes wider and results in narrower resonances. Here, the intensities of the background and resonant scattering become comparable and the phase shift before and after the resonances leads to constructive and destructive interference, producing the asymmetric Fano profiles shown in Fig. 3b. The barrier eventually becomes so wide that tunneling becomes impossible and the resonances die off, ending the first *comb*. The process repeats all over again for each set of higher energy levels, resulting in the sequence of combs. This is shown by $\ell^{(2)} = 31$, which starts the second comb with a Lorentzian resonance. Here, $\ell^{(1)} = 31$ also exists, but does not match the energy of the laser and therefore does not show in Fig. 3b. The evolution of the potential wells of a growing sphere and their energy levels consecutively interacting with the laser is best understood through the video shown in SI.

Fig. 3c shows all the energy levels for a large sphere where three distinct combs are recognizable, 1st in green, 2nd in orange, and 3rd in purple. These show the resonances that would appear for usual spectroscopy where the radius of the sphere is fixed and the wavelength is scanned.

Conclusion

We have revealed a *directional Mie spectrum* with a much simpler structure than previous Mie scattering spectra. The periodic appearance of the Mie resonances provides a ruler to measure the evaporation rates of droplets with nano-metric precision. The huge Q-factor of the resonances in this spectrum make it ideal for biochemical sensors in aerosol science. In particular, it is highly dependent on the refractive index and its spatial distribution, providing a way to measure the concentration of biological or chemical substances, like extracellular vesicles or possibly even viruses, on the surface of evaporating droplets.

Above all, we confirmed that Mie resonances are composed of a series of Fano resonances, found that they are arranged in consecutive combs, and explained all of these characteristics through a quantum mechanical analogy. This makes it possible to explain Mie spectra intuitively, and without the need for computational simulations.

References

- ¹ Mie, G., “Beiträge zur Optik trüber Medien, speziell kolloidaler Metallösungen,” *Annalen der Physik* **330**, pp. 377-445 (1908).
- ² Guimaraes, L. G. & Nussenzeig, H. M., “Theory of Mie resonances and ripple fluctuations,” *Opt. Commun.* **89**, 363–369 (1992).
- ³ Johnson, B. R., “Theory of morphology-dependent resonances: shape resonances and width formulas,” *J. Opt. Soc. Am. A* **10** (2), 343–352 (1993).
- ⁴ Righini, G. C., Dumeige, Y., Feron, P., Ferrari, M., Nunzi Conti, G., Ristic, D. & Soria, S., “Whispering gallery mode microresonators: Fundamentals and applications,” *Rivista del Nuovo Cimento* **34** (7), 435–488 (2011).
- ⁵ Vennes, B. & Preston, C., “Calculating and fitting morphology-dependent resonances of a spherical particle with a concentric spherical shell,” *J. Opt. Soc. Am. A* **36** (12), 2089–2103 (2019).
- ⁶ Kim, W., Özdemir, S. K., Zhu, F., He, L., & Yang, L., “Demonstration of mode splitting in an optical microcavity in aqueous environment,” *Appl. Phys. Lett.* **97** 071111 (2010).

- ⁷ Sonnefraud Y. et al., “Experimental Realization of Subradiant, Superradiant, and Fano Resonances in Ring/Disk Plasmonic Nanocavities,” *ACS Nano* **4** 1664–1670 (2010).
- ⁸ Foreman, M.R., Swaim, J.D., & Vollmer, F., “Whispering gallery mode sensors,” *Adv. Opt. Photonics* **7** 168–240 (2015).
- ⁹ Kiraz, A., Sennaroglu, A., Doganay, S., Dündar, M. A., Kurt, A., Kalaycioglu, H. & Demirel, A. L., “Lasing from single, stationary, dye-doped glycerol/water microdroplets located on a superhydrophobic surface,” *Opt. Commun.* **276** 145–148 (2007).
- ¹⁰ Platts, C. E., M. A. Kaliteevski, S. Brand, R. A. Abram, I. V. Iorsh and, A. V. Kavokin , “Whispering-gallery exciton polaritons in submicron spheres”, *Phys. Rev. B* **79** 24532 (2009).
- ¹¹ A. Canales, D. G. Baranov, T. J. Antosiewicz, and, T. O. Shegai, “Abundance of cavity-free polaritonic states in resonant materials and nanostructures”, *J. Chem. Phys.* **154** 024701 (2021).
- ¹² Ashkin, A. & Dziedzic, J. M., “Observation of Resonances in the Radiation Pressure on Dielectric Spheres,” *Phys. Rev. Lett.* **38** (23), 1351–1354 (1977).
- ¹³ Preston, T. C., Mason, B. J., Reid, J. P., Luckhaus, D. & Signorell R., “Size-dependent position of a single aerosol droplet in a Bessel beam trap,” *J. Opt.* **16** (025702) (2014).
- ¹⁴ Ward, A. D., Zhang, M., & Hunt, O., “Broadband Mie scattering from optically levitated aerosol droplets using a white LED,” *Opt. Express* **16** (21), 16390–16403 (2008).
- ¹⁵ Hart, M. B., Sivaprakasam, V., Eversole, J. D., Johnson, L. J., & Czege, J., “Optical measurements from single levitated particles using a linear electrodynamic quadrupole trap,” *Appl. Opt.* **54** (31), F174–F181 (2015).
- ¹⁶ Archer, J., Kolwas, M., Jakubczyk, D., Derkachov, G., Wozniak, M. & Kolwas, K., “Evolution of radius and light scattering properties of single drying microdroplets of colloidal suspension,” *J. Quant. Spectrosc. Radiat. Transf.* **202**, 168–175 (2017).
- ¹⁷ Willoughby, R. E., Cotterell, M.I., Lin, H., Orr-Ewing, A.J., & Reid J.P., “Measurements of the Imaginary Component of the Refractive Index of Weakly Absorbing Single Aerosol Particles,” *J. Phys. Chem. A* **121** 5700–5710 (2017).
- ¹⁸ Chylek, P., Kiehl, J. T. & Ko, M. K. W., “Optical levitation and partial-wave resonances,” *Phys. Rev. A* **18** (5), 2229–2233 (1978).
- ¹⁹ Price, C. L., Bain, A., Wallace, B. J., Preston, T.C., & Davies, J. F., “Simultaneous Retrieval of the Size and Refractive Index of Suspended Droplets in a Linear Quadrupole Electrodynamic Balance,” *J. Phys. Chem. A* **124** 1811–1820 (2020).
- ²⁰ Limonov, M., Rybin, M., Poddubny, A. et al. “Fano resonances in photonics,” *Nature Photon* **11**, 543–554 (2017).
- ²¹ Rybin, M.V., Samusev, et al., “Mie scattering as a cascade of Fano resonances,” *Opt. Express* **21**, 30107-30113 (2013)
- ²² Tribelsky, M. I. & Miroshnichenko, A. E. “Giant in-particle field concentration and Fano resonances at light scattering by high-refractive index particles,” *Phys. Rev. A* **93**, 053837 (2016).
- ²³ Kong, X. & Xiao, G. “Fano resonance in high-permittivity dielectric spheres. *J. Opt. Soc. Am. A* **33**, 707–711 (2016).

- ²⁴ Fan, X., Zheng, W. & Singh, D. J. , “Light scattering and surface plasmons on small spherical particles,” *Light Sci. Appl.* **3** e179 (2014).
- ²⁵ Tribelsky, M. I. , “Phenomenological approach to light scattering by small particles and directional Fano’s resonances,” *EPL* **104** 34002 (2013).
- ²⁶ Hao, Z., Gao, Y., Huang, Z., Liang, X. & Liu, Y., “Plasmonic Fano switches in Au–SiO₂–Au multilayer nanoshells with broken core,” *Mater. Res. Express* **4** 095006 (2017).
- ²⁷ Mishchenko, M. I., Travis, L. D. & Lacis, A. A., “Scattering, absorption, and emission of light by small particles,” *Cambridge University Press*, United Kingdom (2002).
- ²⁸ Marmolejo, J. T., Urquiza-González, M., Isaksson, O. et al. “Visualizing the electron’s quantization with a ruler,” *Sci Rep* **11**, 10703 (2021).
- ²⁹ Lettieri, T. R., Jenkins, W. D., & Swyt, D. A., “Sizing of individual optically levitated evaporating droplets by measurement of resonances in the polarization ratio,” *Appl. Opt.* **20** (16), 2799–2805 (1981).

Methods

Experimental Setup

We constructed a counter propagating optical trap shown in Fig. 4 using a 532.0 nm, continuous wave, linearly polarized laser (Laser Quantum gem532). We divided the beam into two arms using a polarizing beam splitter (PBS 1) and focused both arms into the same spot from opposite directions inside the trapping chamber. With the $\lambda/2$ wave-plate before PBS 1 we controlled the relative power between both arms. The $\lambda/2$ wave-plate after PBS 1 instead rotated the polarization of the horizontally polarized beam to make both beams be vertically polarized.

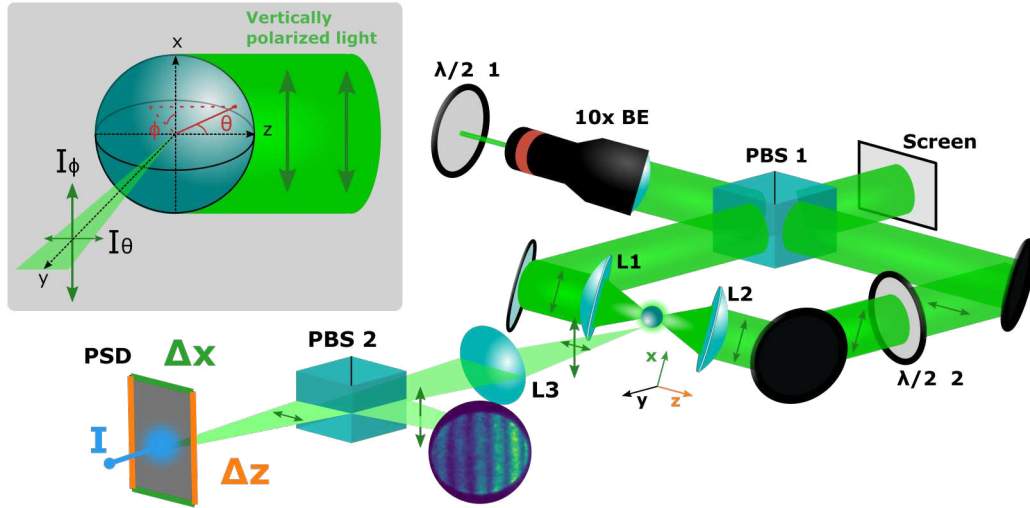


Figure 4: Counter-propagating trap used to record *directional Mie* spectra and evaporation videos of water droplets. Importantly, both laser arms are vertically polarized. A polarizing beam splitter (PBS 2) divided the I_ϕ and I_θ polarization components of the scattering of the droplet. I_θ was focused onto a position sensitive detector (PSD) and I_ϕ was projected onto a transparent screen.

Stable trapping is best achieved when the beam waist of the trapping laser is comparable to the particle size. Therefore, a 10x beam expander was used to turn the beam from a diameter of 0.9 ± 0.1 mm to 9 ± 1 mm. Each arm was then focused using a 100 mm and a 65 mm lens, resulting in beam waists of 7.5 ± 0.8 and 4.9 ± 0.5 , respectively. The dissimilar beam waists were chosen because they expand the range where the beam waist is comparable to the particle size. That is, larger droplets are in the range of the larger beam waist, while the smaller beam waist is comparable to the smaller droplets. Since the cross-section between the droplet and the light changes greatly as the droplet evaporates, a careful balancing between the intensities and alignment of both arms was needed to keep the stability position of the evaporating droplet stable.

We used an ultrasonic nebulizer (MY-520A) to dispense a cloud of water droplets into the trapping chamber. Droplets randomly fell into the optical trap and merged into the largest droplet the trap could hold. After the cloud settled, the remaining droplet quickly evaporated ($\simeq 10$ s).

We collected the light scattered from the droplet using a 50 mm, diffraction limited aspheric lens ($\phi = 25$ mm) placed at a distance $d = 52 \pm 1$ mm away from the droplet perpendicular to the trapping lasers, i.e. $\theta = \phi = \pi/2$, solid angle = 0.174 ± 0.012 sr. We imaged the droplet through a beam splitter (PBS 2) onto a 2D position sensitive detector which recorded the position of the droplet in the y-z plane as well as the total scattering intensity. The inset of Fig. 4 shows the polarization components I_θ and I_ϕ of the scattering perpendicular from the vertically polarized excitation beam.

The reflection from the beam splitter was projected on a screen where the far-field diffraction pattern created by the droplet was visible. We filmed this pattern and used the distance between stripes (S) to calculate the absolute radius of the droplet.

Calculating the energy levels

Following the procedure used by Johnson, B. R.,¹ we obtain the solutions of the Eq.(9) using the quantum analogy expressed in Eq.(11) with the potential in Eq.(10). The solutions for TE modes with the radial function $S_\ell(r)$ obey the Eq.(10). The solutions for the TM modes with the radial function $T_\ell(r)$ take into account the derivative of the refractive index. In our case, the refractive index is a step function and consequently the differential equations are the same except at the boundary of the droplet. Then, the solutions for the radial part, and for each ℓ , are in terms of the regular Riccati-Bessel functions² for $r < a$

$$\Psi_{in} = \psi_\ell(nkr) \quad , \quad (12)$$

and the regular and singular functions for $r > a$

$$\Psi_{out} = B_\ell \psi_\ell(kr) + C_\ell \chi_\ell(kr) \quad . \quad (13)$$

We obtained the matching coefficients B_ℓ and C_ℓ for the two regions with the condition that the wave function and its derivative must be continuous. The resonance condition for each potential is obtained if we extend the potential barrier to infinity where the solutions must have a decreasing exponential behavior. It implies that the coefficient B_ℓ must be zero, and therefore the condition for the resonant states for the TE modes is

$$\psi_\ell(nx)\chi'_\ell(x) - n\psi'_\ell(nx)\chi_\ell(x) = 0 \quad , \quad (14)$$

and for the TM modes is

$$\psi_\ell(nx)\chi'_\ell(x) - \frac{1}{n}\psi'_\ell(nx)\chi_\ell(x) = 0 \quad . \quad (15)$$

where $x = 2\pi a/\lambda = ka$ is the *size parameter*. This parameter highlights the linear relationship between particle radius and excitation wavelength.

For both modes, resonant states can only exist when they are between $k^2(1 - n^2) + \ell(\ell + 1)/a^2$ and $\ell(\ell + 1)/a^2$. With this process we obtained the resonant states for each potential indexed by ℓ .

Subsequently, with a fixed wave number for the laser wavelength of 532.0 nm, we swept the size of the droplet. Consequently, the shape of the potential changes and its corresponding bound states move until the latter coincide with the k^2 value of the laser (see online video). As the droplet grows, it can be observed that when considering the different values of ℓ , the combs corresponding to the different energy levels that are observed in Fig. 3a are formed, which are in agreement with their counterpart in Fig. 2a. We use the colors green, orange and purple in those figures to show this correspondence between experiment and theory. It is worth mentioning that the asymptotic behavior of the condition in Eqs.(14) and (15) for the size parameter x is linear, and this explains the equal spacing between the resonances shown in Fig. 2c.

Data availability

The data shown in this paper as well as the video of the interference fringes of the evaporating droplet can be found [here](#).

References

- ¹ Johnson, B. R., “Theory of morphology-dependent resonances: shape resonances and width formulas,” *J. Opt. Soc. Am. A* **10** (2), 343–352 (1993).
- ² Olver, F. , Lozier, D. , Boisvert, R. & Clark, C., “The NIST Handbook of Mathematical Functions,” *Cambridge University Press*, New York, (2021).

Acknowledgements

Financial support from the Swedish Research Council (2019-02376) is acknowledged. R.M.-F. acknowledges the financial support from The Wenner-Gren Foundations and the grants DGAPA-PASPA, PAPIIT-IN-112721 and PAPIME-PE-103021. We thank Mats Rostedt for his help with I.T.

Author contributions

D.H. coordinated the project. J.T.M. built the experimental system, conducted the experiments, and analyzed the data. All authors contributed to the theoretical explanation. R.M.-F. performed the numerical calculations. J.T.M. and R.M.-F. wrote the draft of the manuscript. All authors contributed to the final version of the manuscript.

Competing interests

The authors declare no competing interests.

Materials & Correspondence

Contact J.T.M. at javier.marmolejo@physics.gu.se .

Supplementary Files

This is a list of supplementary files associated with this preprint. Click to download.

- [SIMarmolejo.pdf](#)
- [VideoMarmolejo.mp4](#)